JOURNAL OF THEORETICAL AND APPLIED MECHANICS
62, 4, pp. 769-786, Warsaw 2024
https://doi.org/10.15632/jtam-pl/195069

INFLUENCE OF GEOMETRICAL DEFECTS ON AERODYNAMIC DRAG OF NON-WATERTIGHT AHMED BODY

Xuelong Liu
Tianjin University, Tianjin, China; and
CATARC (Tianjin) Automotive Engineering Research Institute Co., Ltd., Tianjin, China
e-mail: lixuelong@catarc.ac.cn

Haidong Yuan, Qing Qin
CATARC (Tianjin) Automotive Engineering Research Institute Co., Ltd., Tianjin, China
e-mail: yuanhaidong@catarc.ac.cn; qinqing@catarc.ac.cn

Songze Chen
Shenzhen Tenfong Technology Co., Ltd., Shenzhen, China
e-mail: chensz@tenfong.cn

A non-watertight Ahmed body is adopted to examine the influence of geometrical defects on the aerodynamic drag. The Ahmed body, a standard automotive test model, is widely used in wind tunnel experiments to study vehicle aerodynamics. However, in real-world applications, vehicles often exhibit deviations from the ideal geometry due to manufacturing tolerances, wear, and other factors. The aim of this study is to quantify the impact of such geometrical defects on the aerodynamic drag. The research employs the lattice Boltzmann method (LBM) software to analyze the flow field around the Ahmed body with and without the introduction of geometrical defects. These defects are modeled as small holes in the shape of the body. The simulations are performed under the varying location and size of the holes to explore the aerodynamics phenomena. The results indicate that the location and size of geometrical defects can significantly alter the aerodynamic drag of the Ahmed body. The holes located at the rear of the Ahmed body rarely effect the aerodynamic drag. The holes at the top or bottom are found to have the most pronounced effect. The study also reveals that the influence of defects varies with their size, with large areas leading to more substantial changes in the aerodynamic drag. The results demonstrate that non-watertight geometry with small defects can be used to produce a reasonable drag coefficient compared to the results of watertight geometry.

Keywords: Ahmed body, non-watertight geometry, aerodynamic drag

1. Introduction

The Ahmed body is a highly recognized testing apparatus in automotive aerodynamics. It serves as a simplified yet representative model of a passenger car for studying aerodynamic drag and flow characteristics. It was originally designed by Ahmed *et al.* (1984). The Ahmed body exhibits a distinct shape that closely resembles the fundamental contours of a real-world car. Its front section is flat and connected with the rectangle body by a curved surface. The most notable feature of the Ahmed body is its truncated rear end, which is characterized by a slant angle that can be adjusted to simulate different rear geometries of cars.

Many scholars and researchers conducted wind tunnel experiments on the Ahmed body with different rear slant angles. Ahmed *et al.* (1984) measured the drag coefficient and pressure distribution for different rear slant angles from 0° to 40°, showing complex flow phenomena at the rear. Bayraktar *et al.* (2001) conducted experiments with different Reynolds numbers in the

range of $2.2M$ to $13.2M$ for models with different rear slant angles of 0°, 12.5° and 25° and yaw angles between −15° to 15°, and compared their effects on the force and flow field of the model. Lienhart and Becker (2003) provided supplementary statistical data on average velocity distribution, average pressure distribution, and turbulent high-order quantities for their model experiments with rear slant angles of 25° and 35°. Strachan *et al.* (2007) compared the effects of static and moving ground on the drag coefficient and flow field of the model with a rear slant angle of 0° to 40°.

In addition to the above mentioned and many other experimental studies (ERCOFTAC, 2023), plenty of numerical simulations (Han, 1989; Gilliéron and Chometon, 1999; Keating *et al.*, 2008; Holman *et al.*, 2012) including LBM (Keating *et al.*, 2008; Fares, 2006; Kotapati *et al.*, 2009) were conducted for further exploration of the Ahmed body.

Han (1989), Gilliéron and Chometon (1999), Keating *et al.* (2008), Holman *et al.* (2012) comprehensively replicated the distinct drag coefficient characteristics of the Ahmed body in details. From 0° to approximately 9°, the drag coefficient of the Ahmed body decreases as the slant angle increases. Then it increases with an increase of the slant angle, and the drag coefficient reaches the highest value when it reaches 30°. When the slant angle is greater than 30°, the wake changes greatly, resulting in a sudden drop in the drag coefficient. In numerous numerical simulations, the Ahmed body serves as a simplified model for verification. Nonetheless, literature and technical reports rarely discuss real-world geometric imperfections in numerical studies. Perhaps, required by many numerical methods, the geometry had to be watertight. Any geometric imperfections or defects are corrected in advance. The aerodynamics of non-watertight geometry with geometrical defects was rarely explored in the past.

It is worth noting that the aerodynamic feature of non-watertight geometry also plays a crucial role in automotive design. Unlike simple geometries, say, sphere or cylinder, most geometries of the vehicle have many components. The assembly errors are common, and will make many small cracks or holes in the surface. Some of these defects are solely computational, but some are really generated in the manufacturing process. At present, almost all cracks and holes that prevent the geometry from being watertight are repaired or fixed in the preprocessing phase, regardless of whether they are real or computational.

In this article, we delve into the drag coefficient of the non-watertight Ahmed body. To assess its sensitivity, we introduce various types of openings into the surface of the standard Ahmed body, adjusting their sizes and locations. Our objective is to discern the key factor that significantly impacts the drag coefficient and identify which imperfections have a minimal effect. By analyzing the simulation results, we aim to determine the primary influence on the drag coefficient.

To achieve our goal, it is imperative to employ a CFD solver capable of handling non--watertight geometries. Therefore, we opt for TF-Lattice, a CFD software that utilizes the Lattice Boltzmann Method (LBM) (Qian *et al.*, 1992; Chen and Doolen, 1998; Jacob *et al.*, 2018). The grid system in TF-Lattice provides a flexible framework to represent non-watertight surfaces. A concise overview of TF-Lattice, along with its validation, is provided in the Appendix for further reference.

2. Geometric model

2.1. Standard Ahmed body with different rear slant angles

Reproduce the baseline results and validate the software.

Ahead of the non-watertight geometry, the standard Ahmed bodies with different rear slant angles are simulated by TF-Lattice to reproduce the baseline results achieved in the previous research to ensure the consistency and reliability of the software. By validating the software

against these established benchmarks (Ahmed *et al.*, 1984; Keating *et al.*, 2008; Hinterberger *et al.*, 2004), we aim to provide confidence of the software accuracy, robustness, and ability to perform as expected. A sketch of the Ahmed body (Hinterberger *et al.*, 2004) is shown in Fig. 1, which exhibits different vortices, separation, and reattachment phenomena at different rear slant angles. The length of the model is $L = 1.044\,\mathrm{m}$, the width $W = 0.389\,\mathrm{m}$, the height $H = 0.288\,\mathrm{m}$, and the ground clearance is $0.05\,\mathrm{m}$. There are four cylindrical support rods with a diameter of $0.03\,\mathrm{m}$ located between the bottom of the model and the ground. The simulation results of the drag coefficient and flow state will be present at four slant angles of 0°, 12.5°, 25° and 35°.

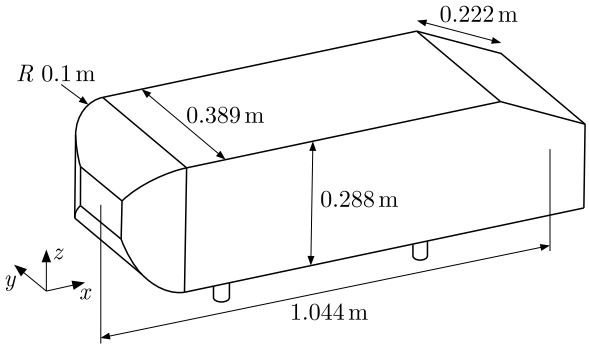

Fig. 1. Sketch of the Ahmed body

2.2. Non-watertight Ahmed body of 0° slant angle

To investigate the effect of geometrical defects on the drag coefficient, we introduced openings at various locations in the standard Ahmed body with a 0° slant angle, specifically in its upper surface, lower surface, lateral surface, and rear surface. We perform a series of numerical simulations, varying the area and distribution of the openings, with a particular emphasis on the lower surface. This focus is based on the recognition that the chassis section is the most intricate component of a vehicle and is where geometrical defects are most likely to occur. Therefore, our case studies concentrate on examining various configurations of the openings in the lower surface. The specific opening locations and corresponding parameters are shown in Table 1, and 3D views of various opening situations are shown in Fig. 2.

Table 1. Setup for the non-watertight Ahmed bodies

Case	Hole location	Area ratio (hole area/face area)
1	None	–
2	Top	10%
3	Lateral	10%
4	Rear	10%
5	Bottom	10%
6	Bottom	5%
7	Bottom	1% × 5
8	Bottom	1%

3. Computational settings

The computational domain is established as shown in Fig. 3. The total length of the computational domain is $10L$, where L represents length of the Ahmed body. The inlet of computational domain is located at $2L$ in front of the Ahmed body, and the outlet is located at $7L$ behind the

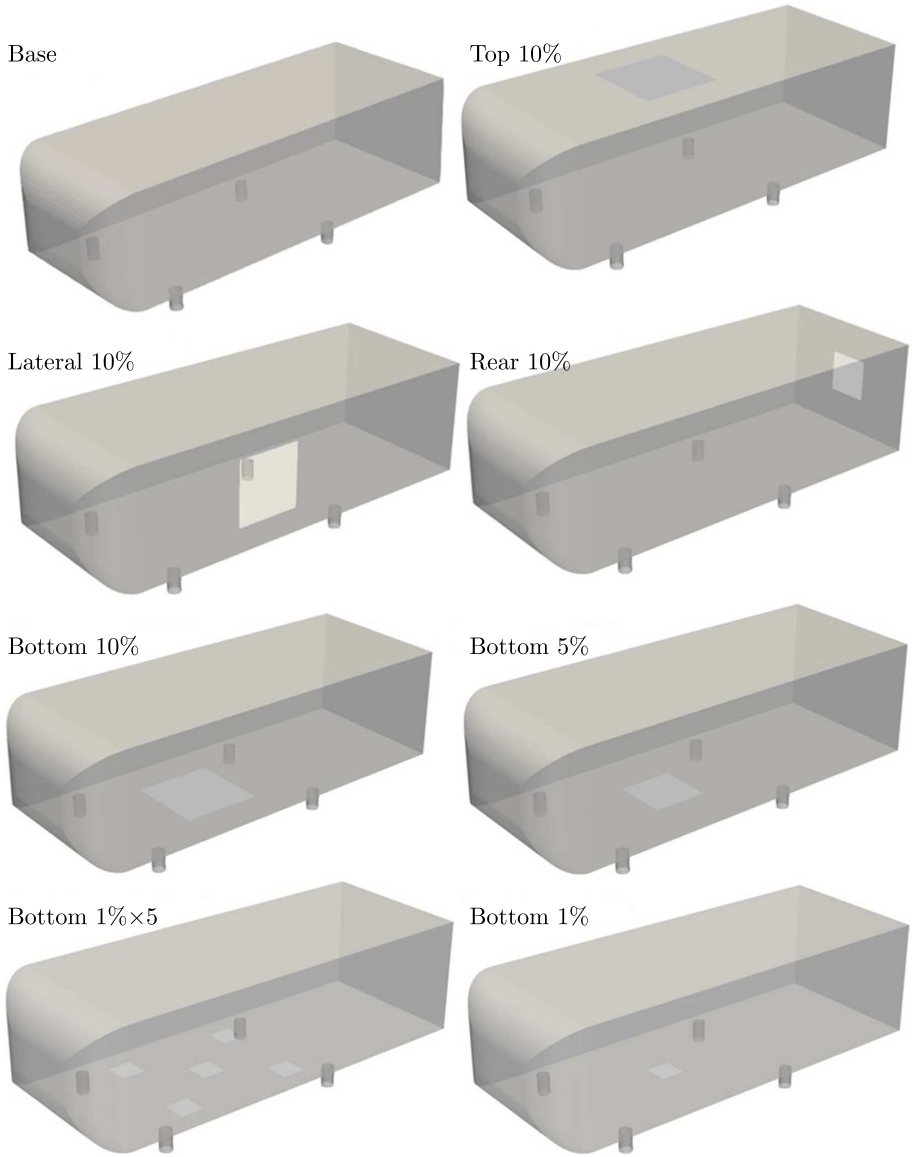

Fig. 2. Illustrations of the non-watertight Ahmed bodies (slant angle = 0°)

Ahmed body. The rear wake area is long enough to ensure that the wake is fully developed. The total domain width is $8W$, the height of computational domain is $9H$, and the blockage ratio of the whole model is 1.4%, which is a common blockage ratio in a wind tunnel.

Boundary conditions are exhibited in Table 2. The Reynolds number of the flow, which is about 4×10^5, is estimated with the incoming flow velocity of 20 m/s, air viscosity and the height H of the Ahmed body.

Table 2. Boundary conditions

Boundary name	Boundary condition
Outlet	Uniform velocity inlet of 20 m/s
Inlet	Far field
Spanwise and upper faces	Symmetry
Ground	Fixed no-slip wall
Ahmed body	Fixed no-slip wall

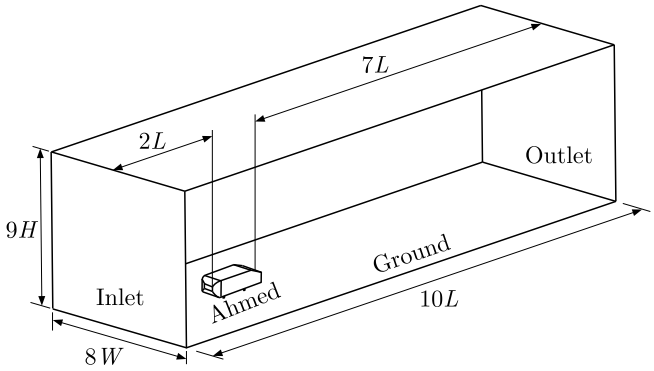

Fig. 3. Illustration of the simulation domain

A multilayer grid is generated to ensure that near wall areas are discretized with a fine grid size, and the outer areas are discretized with a relatively coarse grid size to save computation resources. Specifically, the computational domain is divided into six layers. The coarsest grid size among these layers is 0.0768 m, and is located at the outer areas of the computational domain. The finest grid distributes around the surface of the Ahmed body, its size is 0.0024 m. The total grid volume is about 11 million. Figure 4 shows the grid of the computational domain in $Y = 0$.

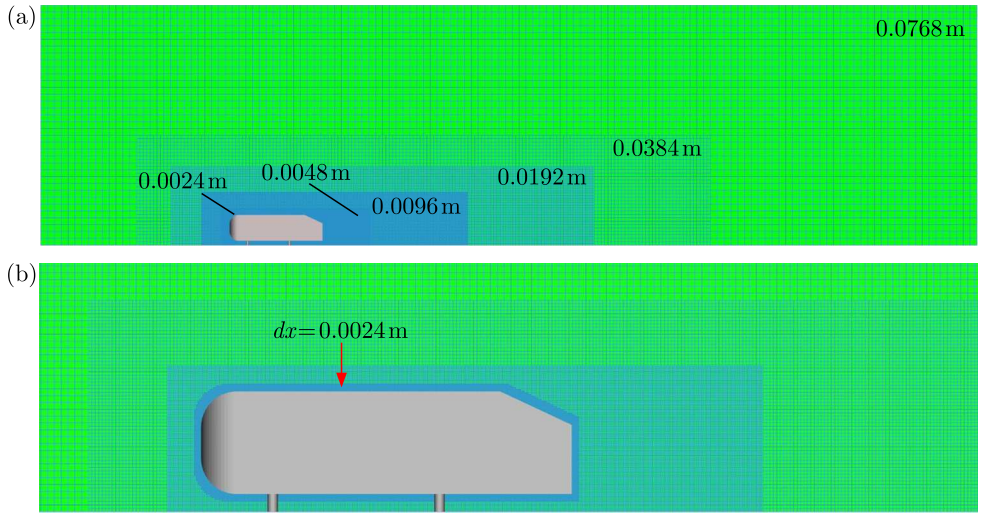

Fig. 4. Grid of the computational domain in $Y = 0$: (a) grid of the domain in $Y = 0$ slice, (b) multilayer grid around the Ahmed body in $Y = 0$ slice

The simulations were conducted on a 128-core CPU (AMD EPYC 7H12 64-Core Processor x2). The initial flow field is set as a uniform flow with a constant velocity and density, except for a box area enclosing the Ahmed body. In the small box around the Ahmed body, the initial flow is set to zero velocity to avoid the transient oscillation inside the Ahmed body. The calculated physical duration is 1 s (the fluid sweeps about 10 body lengths).

4. Results and discussion

4.1. Standard Ahmed body with different rear slant angles

4.1.1. Velocity distribution and pressure distribution

Figure 5 and 6 show the average velocity field, pressure distribution and streamlines of the central section of the model with different rear slant angles $Y = 0$ in the period of 0.75 s-1.0 s, and

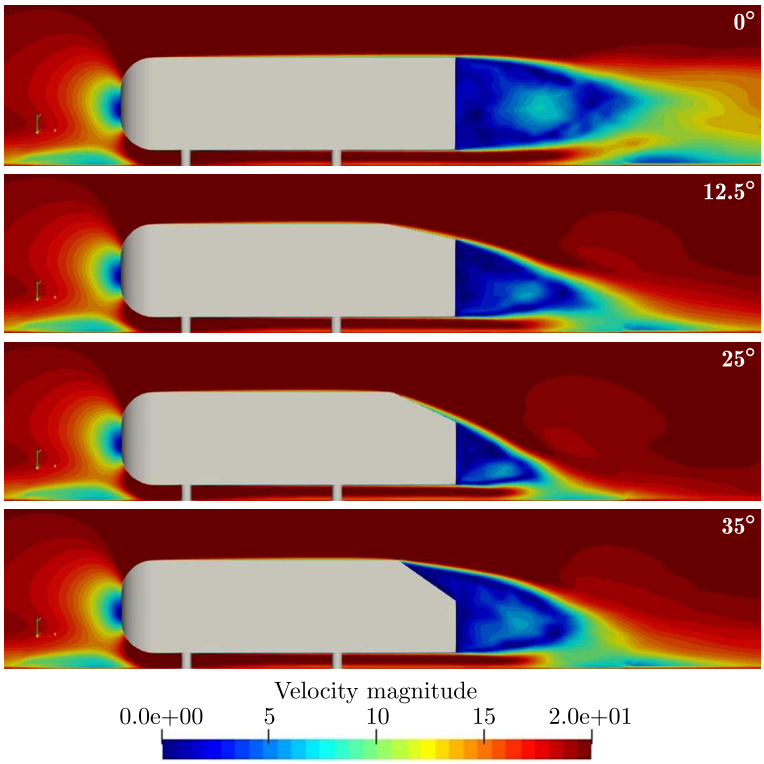

Fig. 5. Time averaged velocity field in $Y = 0$ slice

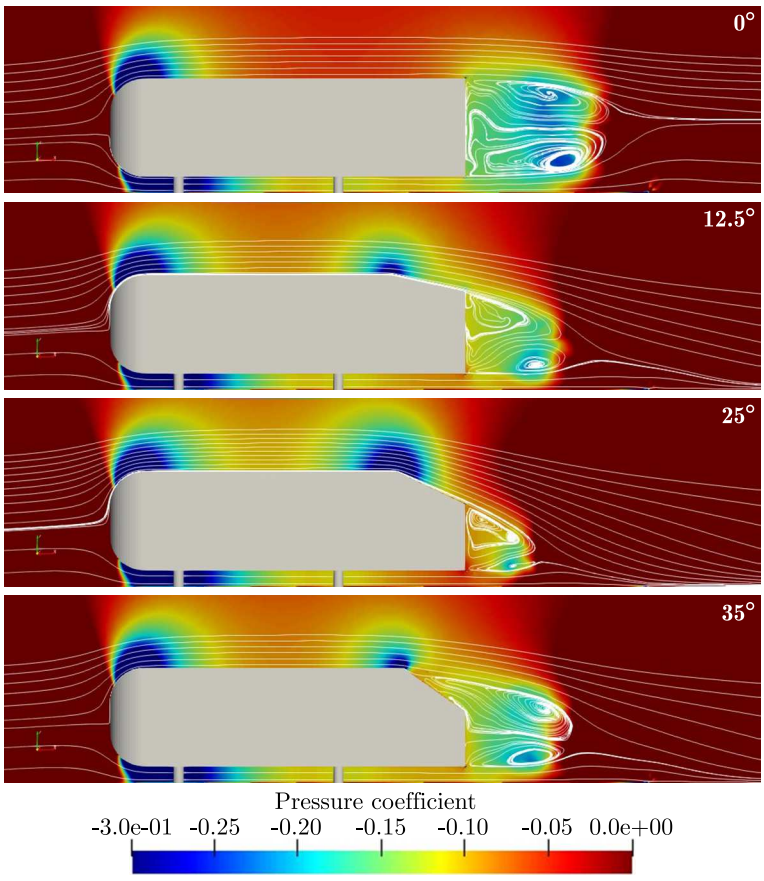

Fig. 6. Pressure coefficient and streamline in $Y = 0$ slice

Fig. 7 shows the iso-surfaces with the total pressure of 0. The velocity and pressure distributions from the head of the model to the rear slant are basically the same in the four simulations. Under the condition of the rear slant angle of 0°, our simulation results show that the rear presents a relatively stable wake vortex far away from the rear part. The flow at a slant angle of 12.5° is similar to the experimental results (Ahmed, *et al.* 1984) and simulation results (Keating *et al.*, 2008): the airflow remains attached at the top corner, and only separates at the end of the rear; the wake vortex at the rear becomes smaller than that of the 0° slant angle. The pressure decreases in a small area near the top corner. As the slant angle increases to 25°, experiments (Bayraktar *et al.*, 2001) and other simulation results (Keogh *et al.*, 2016) show that the airflow separates at the top and then reattaches the surface at about 1/2 way down the slant. A large area of low pressure appears near the top corner of the model. When the slant angle is 35°, the simulation results show that the air flow at the top of the model is cleanly separated, and the wake vortex is far away from the rear.

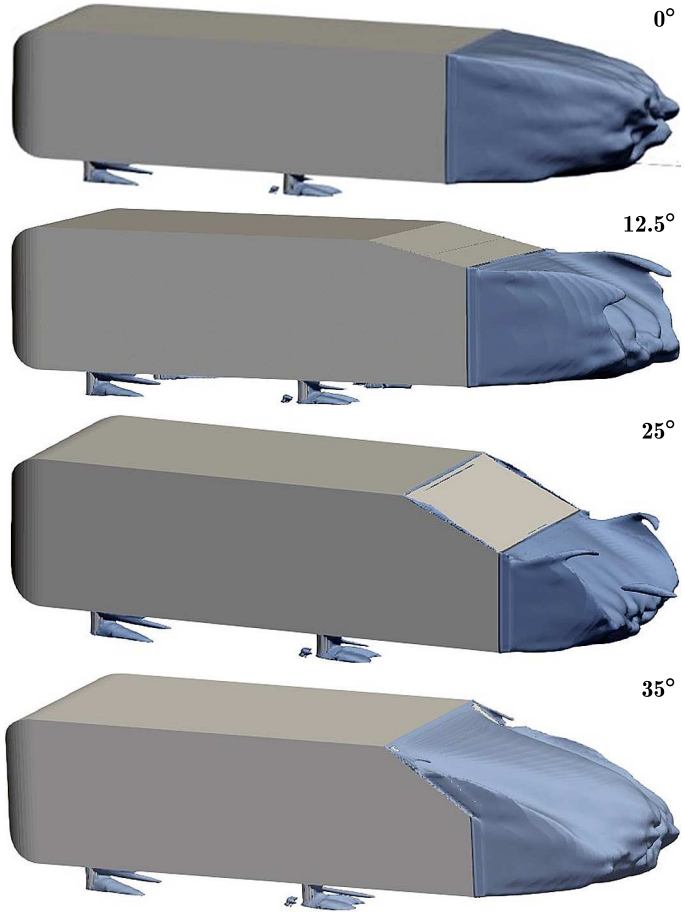

Fig. 7. Zero total pressure contour

4.1.2. Drag coefficient

According to the experimental findings reported by Ahmed *et al.* (1984), it is evident that under identical conditions, the drag coefficient exhibits a distinct trend with respect to the rear slant angle of the Ahmed body. Specifically, as the slant angle increases from a smaller value, the drag coefficient also increases, exhibiting a positive correlation up to a threshold of 30°. However, once the slant angle surpasses this critical point of 30°, the drag coefficient undergoes a sharp decline, plummeting to a significantly lower value. This indicates a significant drop in the drag resistance as the slant angle exceeds 30°. Table 3 lists the drag coefficients of the Ahmed body

with different slant angles obtained by TF-Lattice, PowerFLOW v4.0 (Kotapati *et al.*, 2009) and the experiment conducted by Ahmed *et al.* (1984). These data are also plotted in Fig. 8 for comparison. We can find that the trend of the drag coefficient obtained by TF-Lattice with the slant angle is consistent with the experiment and former simulation, and the error to the experimental results is within 5%.

Table 3. Drag coefficient of Ahmed bodies

Slant angle	0°	12.5°	25°	35°
TF-Lattice C_D	0.247	0.238	0.271	0.249
Ahmed *et al.* (1984) C_D	0.250	0.230	0.285	0.260
PowerFLOW C_D	–	0.237	0.316	0.278

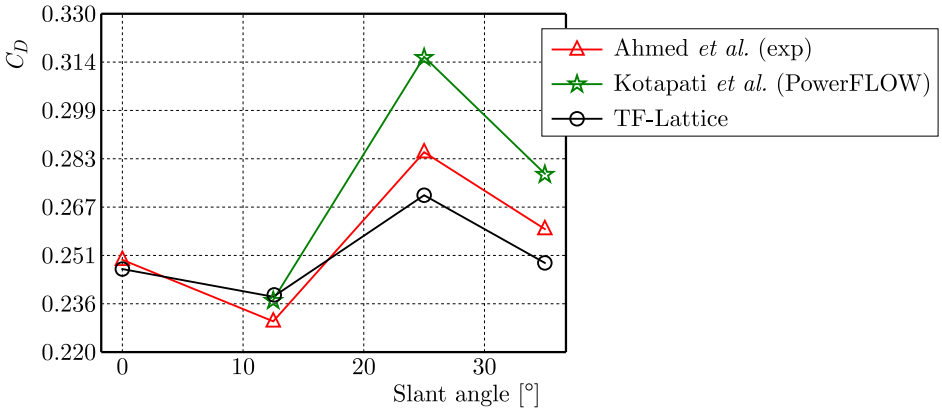

Fig. 8. Drag coefficient of Ahmed bodies with different slant angles

4.2. Non-watertight Ahmed body of 0° rear slant angle

This Section focuses on exploring the aerodynamics of a non-watertight Ahmed body with the aim of identifying the most significant factor that influences its drag coefficient.

4.2.1. Pressure distribution

When simulating the aerodynamics of a non-watertight Ahmed body, a significant alteration is observed in the pressure distribution within the structure. This change in pressure distribution is a notable consequence of the opening in the surface. Figure 9 shows the average pressure distribution and streamline of the $Y = 0$ slice of the Ahmed body in the 0.75 s-1.0 s time periods. The first row in Fig. 9 shows that the internal pressure keeps constant during the simulation for the watertight Ahmed body. It can be seen from the figures that the streamlines enter the interior of the model from the opening. Different opening location leads to different flow patterns inside the model. As the opening exists, the internal pressure drops, even the area ratios of the opening decrease to 1%, the pressure also drops dramatically. In fact, the pressure balance to the adjacent outer flow pressure will establish through the openings.

Besides the pressure drop inside the Ahmed body, the uniformity of the pressure field is obviously different from each other. As the base line simulation, the interior of watertight Ahmed body is very uniform in terms of pressure distribution. We can also find that in the rear 10% and bottom 1% cases the pressure is also uniformm despite the pressure decrease is different in each case. In the other cases, pressure distribution becomes nonuniform. In fact, the pressure

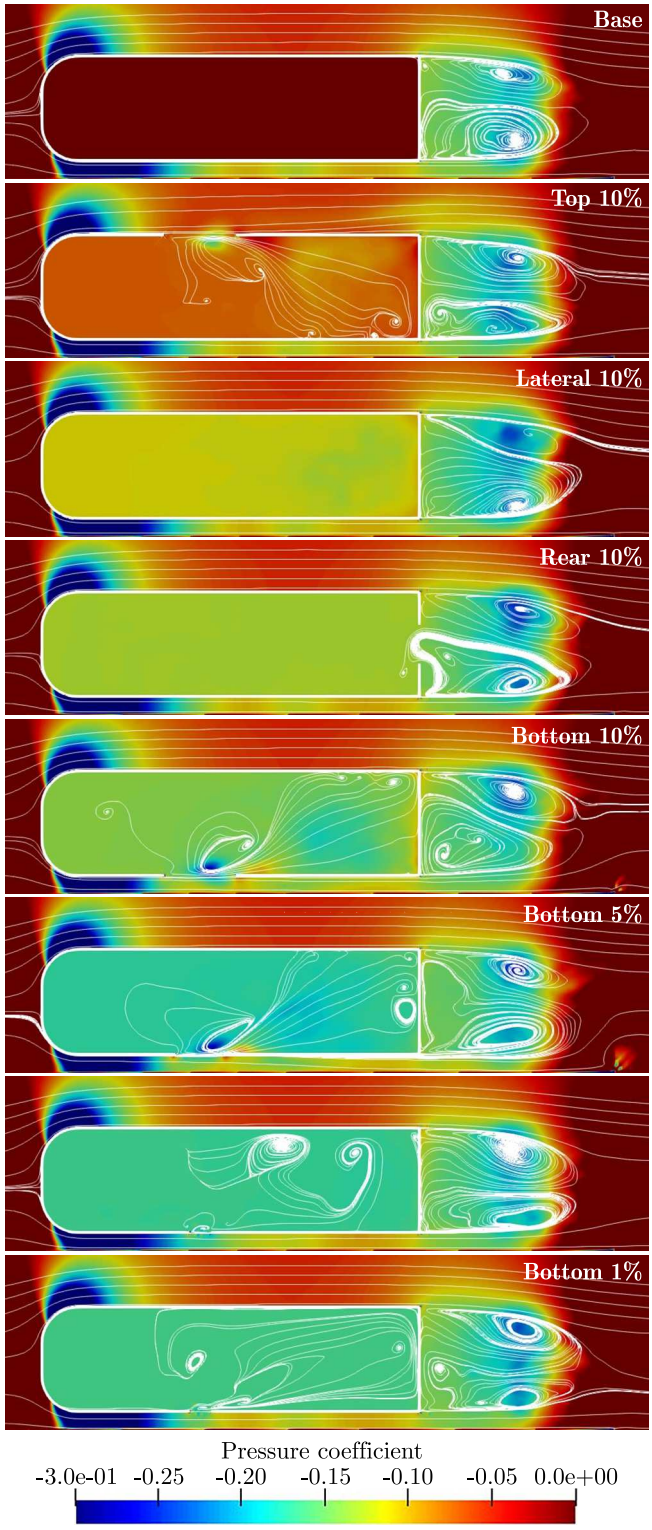

Fig. 9. Pressure coefficient and the streamline in $Y = 0$ slice

distribution is highly dependent on the flow patterns inside the Ahmed body. With large area ratios, the flow passage is large and vortex shedding is strong at the openings. Therefore, the flow patterns become strong and energetic. These phenomena are also reflected in the drag coefficient curves.

4.2.2. Drag coefficient

The pressure distribution inside the Ahmed body will influence the drag coefficient. However, the pressure decrease in the interior is almost irrelevant to the changes of the drag coefficient.

Figure 10 shows the temporal variation curve of the drag coefficient under various geometry configurations (two figures in vertical is a group, the upper one exhibits the complete curve from 0-1.0 s, and the lower one plots the enlarged curve from 0.75 s-1.0 s). To compare the drag coefficients, the range of the vertical axis is set to be of the same scale. The drag coefficient of the watertight Ahmed body fluctuates around the mean value at the beginning of simulation, and after the flow field stabilizes, the variation of the drag coefficient is only ± 0.02.

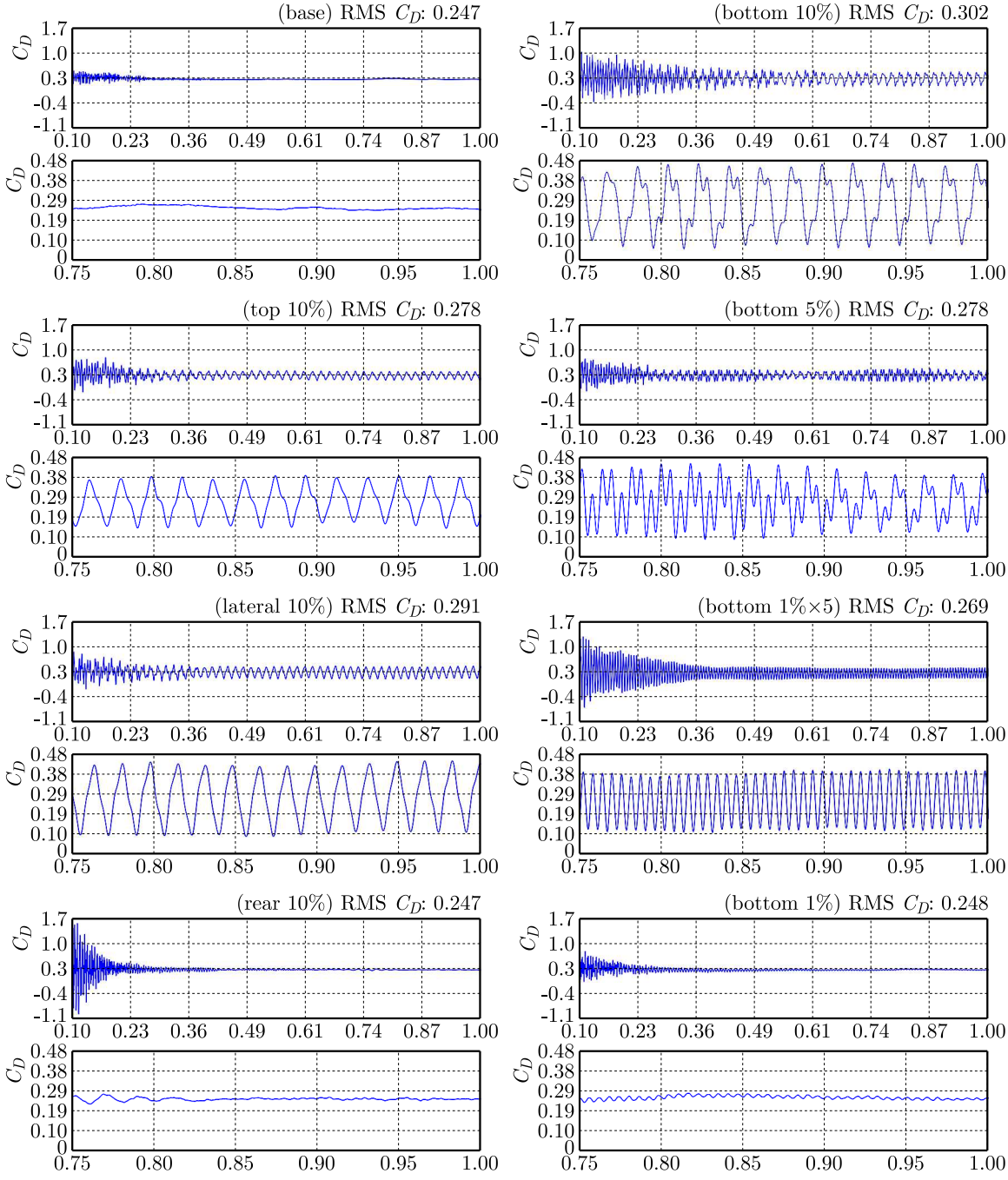

Fig. 10. Evolution of the drag coefficient with time

It worth to note two cases in Fig. 10, rear 10% and bottom 1%, in which the drag coefficient is almost unchanged compared to the base simulation. The pressure decrease in the bottom 1% case is even strongest among the others. In addition, the pressure is uniform inside the Ahmed body for these two cases.

In fact, the uniform pressure decrease inside the geometry will not result in changes in the drag coefficient. Since the pressure is balanced at the opening, and the integral of aerodynamic force in internal surface is identical to the integral in the outer surface of the opening. As illustrated in Fig. 11, the pressure force exerted on the geometry can be calculated as follows

$$F_p = \int\limits_{\Omega_{ex}} -np\, dS + \int\limits_{\Omega_{in}} np\, dS \tag{4.1}$$

Considering the pressure balance at the opening area and Gauss formula, we have

$$\begin{aligned} 0 &= \int\limits_{\Omega_{o,in}} -n_o p\, dS + \int\limits_{\Omega_{o,ex}} n_o p\, dS \\ 0 &= \int\limits_{\Omega_{in}} -np\, dS + \int\limits_{\Omega_{o,in}} -n_o p\, dS \end{aligned} \tag{4.2}$$

Therefore

$$F_p = \int\limits_{\Omega_{ex}} np\, dS + \int\limits_{\Omega_{o,ex}} n_o p\, dS \tag{4.3}$$

It means the pressure force exerted on the non-watertight geometry is identical to the pressure force exerted on the watertight geometry if the external flow is identical. Since the friction force generally is small and the opening area could be small too, we neglect the friction force in this discussion. Accordingly, the discussion for the pressure force is extended to the total aerodynamic force hereafter.

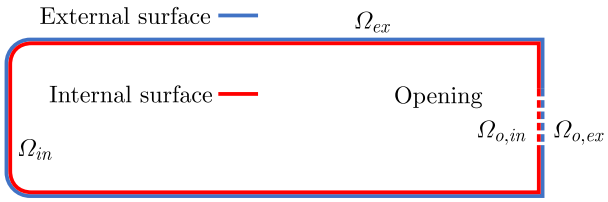

Fig. 11. The surface of the non-watertight model

How small the opening area ratio needs to be is dependent on its specific location in the surface. As four cases with the 10% opening area ratio demonstrate, 10% is small enough when the opening locates at the rear part of the Ahmed body. It is because that the flow at the rear is slow and with moderate pressure variation. Although the opening area seems large, the flow keeps almost quiescent inside the Ahmed body. On the contrary, the other three openings locate at top, bottom and side, where the stream is very strong. Consequently, the massive flow passes through the opening, disturbs the internal pressure distribution and external main flow, and leads to a change in the drag coefficient.

Figure 12 compares the average drag coefficient (0.5-1.0 s) under various geometrical defects, and the specific values are listed in Table 4. In the case of the same opening area, the bottom opening has the most obvious effect. And when the area at the bottom is smaller, the drag coefficient is lower. With the 5% area ratio at the bottom, if the opening area are scattered

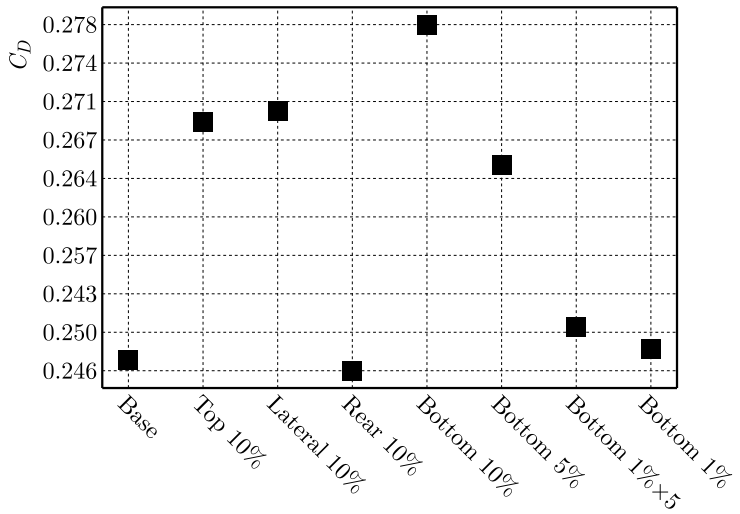

Fig. 12. Drag coefficient of different non-watertight models

Table 4. Drag coefficient of different cases

Case	Base	Top 10%	Lateral 10%	Rear 10%
C_D	0.247	0.278	0.291	0.247

Case	Bottom			
	10%	10%	1% × 5	1%
C_D	0.302	0.278	0.269	0.248

(bottom 1% × 5) at the bottom, the drag coefficient will be lower than that of a single opening (bottom 5%).

Based on the previous discussion, it can be concluded that the increase of the drag coefficient of the Ahmed body is inversely correlated to the uniformity of pressure distribution within it. Specifically, when the pressure distribution inside the Ahmed body is more uniform, the drag coefficient experiences lesser variations. Conversely, as the internal flow disturbance increases and the pressure distribution becomes more uneven, the drag coefficient rises significantly. This phenomenon underscores the importance of optimizing the pressure distribution and minimizing flow disturbances within the Ahmed body to achieve lower drag coefficients.

5. Conclusion

This study first validated the TF Lattice's capability in simulating the drag coefficient of the standard Ahmed body through comparison with the established experimental data. For slant angles of 0°, 12.5°, 25° and 35°, the simulation results of TF Lattice are in good agreement with the literature results. Especially, it is almost identical to the experimental results when the back angle is 0°.

After that, to examine the influence of geometric defects on the drag coefficient, non--watertight Ahmed bodies were created by introducing square holes into the standard Ahmed body with a rear slant angle of 0°, which were then used in further case study simulations.

Based on the simulation results, the geometrical defects have great influence on the drag coefficient. The influence path is identified as follows: Initially, defects or openings in the Ahmed body create a connection between its exterior and interior, allowing for pressure equilibration at these openings. Consequently, this leads to a reduction in the internal pressure. It is important

to note that a uniform decrease in pressure does not alter the drag coefficient. It is only when the opening is significant or the external flow stream is intense so non-uniformities arise in the pressure field, ultimately causing a rise in the drag coefficient.

These phenomena imply that the location of the opening is an important factor that determines how crucial is the opening area effect on the drag coefficient. In general, the larger the opening area is, the greater change of the drag coefficient will be. Meanwhile, provided that the opening area is enough small, the non-watertight geometry can reproduce the drag coefficient derived by watertight geometry.

Non-watertight geometry is natural and ubiquitous in engineering. In the past, most CFD simulations need preprocessing to enclose the geometry which is time consuming and expensive. The results and discussion in this study show another promising way which directly solves flow problems on non-watertight geometry, and which deserves more attention and further investigation.

Appendix

A.1. Flow solver

We employed a newly emerging lattice Boltzmann method (LBM) based software, TF-Lattice V1.0, as the flow solver in this study. LBM is very suitable for solving unsteady problems, such as high Reynolds number flows. Commercial CFD software based on LBM, including PowerFLOW (Dassault) and Ultra Fluid X (Altair), has become an important tool in the automobile industry. The TF-Lattice is another LBM based CFD software developed by Tenfeng Technology in China. It utilizes a multi-layer Cartesian grid to discretize the space, and a cutting cell technique to handle an arbitrary curved surface. Therefore, the TF-Lattice is capable of simulating on a non--watertight geometry with various kinds of geometric defects, such as punctures, small cracks, overlapping surfaces, etc., and can be used directly in simulation. This feature is a perfect match for our researches.

A.2. Lattice-Boltzmann method

For the sake of completeness, the numerical method in TF-Lattice is briefly introduced. LBM is an explicit mesoscopic method that simulates the fluid motion by imitating particle stream and collision. The evolution equation of the lattice Boltzmann method is actually a special discrete form of the kinetic equation in a specific velocity space (He and Luo, 1997)

$$f_i(x + c_i\, dt, t + \Delta t) - f_i(x,t) = -\frac{1}{\tau}[f_i(x,t) - f_i^{eq}(x,t)] \tag{A.1}$$

where f is the velocity distribution function which depends on location x, time t and particle discrete velocity c_i. The subscript i represents a group of discrete velocity directions. Common discrete velocity models include D2Q7, D2Q9, D3Q15, and D3Q19 (Qian *et al.*, 1992). The D3Q19 discrete velocity model is employed in TF-Lattice.

The right-hand side of Eq. (A.1) is solved by a collision model called Hybrid Recursive Regularization (Jacob *et al.*, 2018). This model combines the standard BGK (Bhatnaga *et al.*, 1954) single relaxation, regularization procedure and a distribution function reconstructed from finite difference scheme together. This model can effectively suppress non-hydrodynamic modes generated by LBM in high Reynolds number flows (Jacob *et al.*, 2018; Malaspinas, 2015). In TF-Lattice, the hybrid part of HRR is replaced by a reconstructed distribution function invented by Tenfong Technology. For more information about the LBM, please refer to the special articles (Qian *et al.*, 1992; Chen and Doolen, 1998; Jacob *et al.*, 2018) and references therein.

A.3. Validation

The software, TF-Lattice, was validated by many test cases. Most of the following testing results are excerpted from the internal technical report of TF-Lattice software.

A.3.1. Laminar flow past sphere

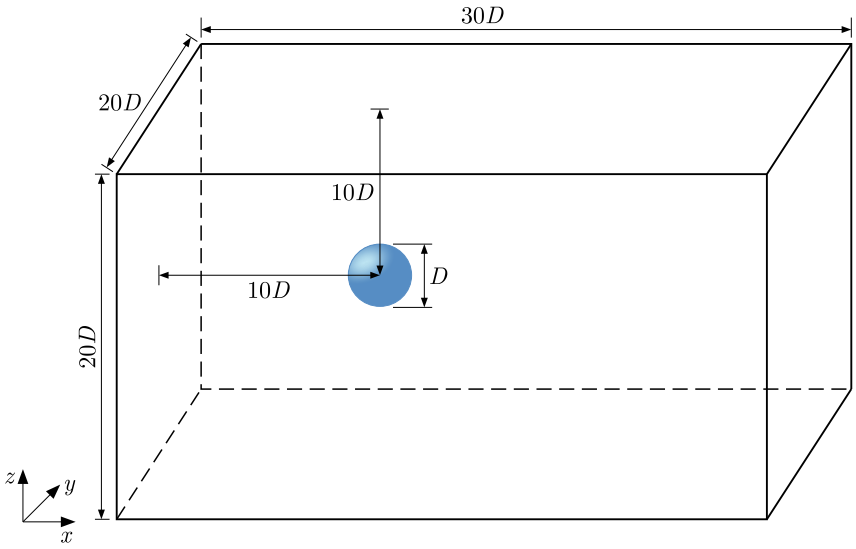

Fig. 13. Configuration of the flow past sphere

Table 5. Drag coefficient of the sphere at different Reynolds numbers

Re	TF--Lattice	Schiller and Naumann (1933)	Johnson and Patel (1999)	Nagata *et al.* (2016)	Sheard *et al.* (2005)	Average	Error
50	1.5774	1.5381	1.58	1.54	1.59	1.5620	0.99%
100	1.0918	1.0917	1.09	1.07	1.09	1.0854	0.58%
200	0.7915	0.8056	0.78	0.76	0.77	0.7789	1.62%

A.3.2. Laminar flow past sphere

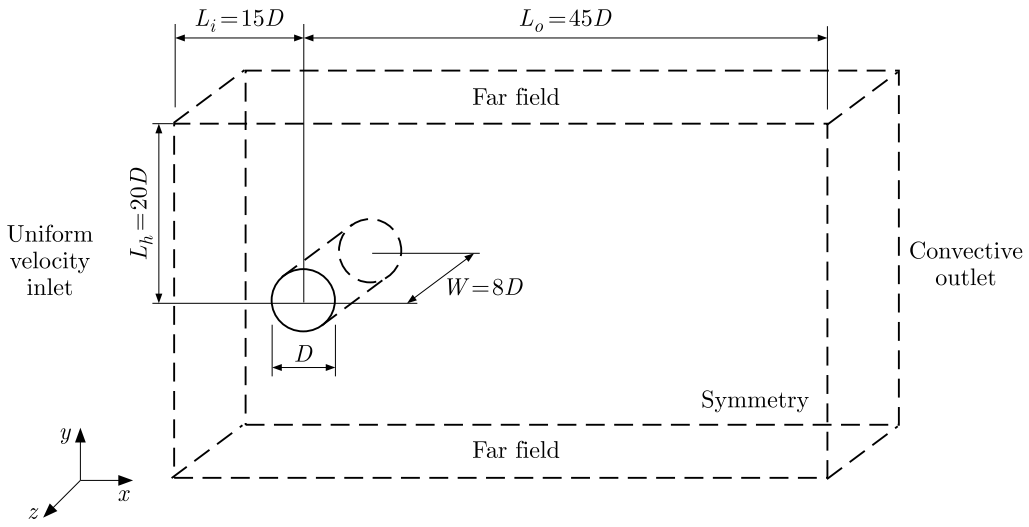

Fig. 14. Configuration of a flow past cylinder

Table 6. Drag coefficient of the cylinder at different Reynolds numbers

Drag coefficient	Reynolds number				
	20	40	60	80	100
Takami & Keller	2.00	1.54	1.32	–	–
S.C.R. Dennis	2.05	1.52	–	–	1.06
Nieuwstadt & Keller	2.05	1.55	–	–	–
M. Nishioka	1.94	1.47	1.31	–	–
R. Franke	–	–	1.35	1.35	–
J. Park	2.01	1.51	1.39	1.35	1.33
TF-Lattice	2.09	1.57	1.36	1.32	1.29

A.3.3. Flow past sphere at Re = 10000

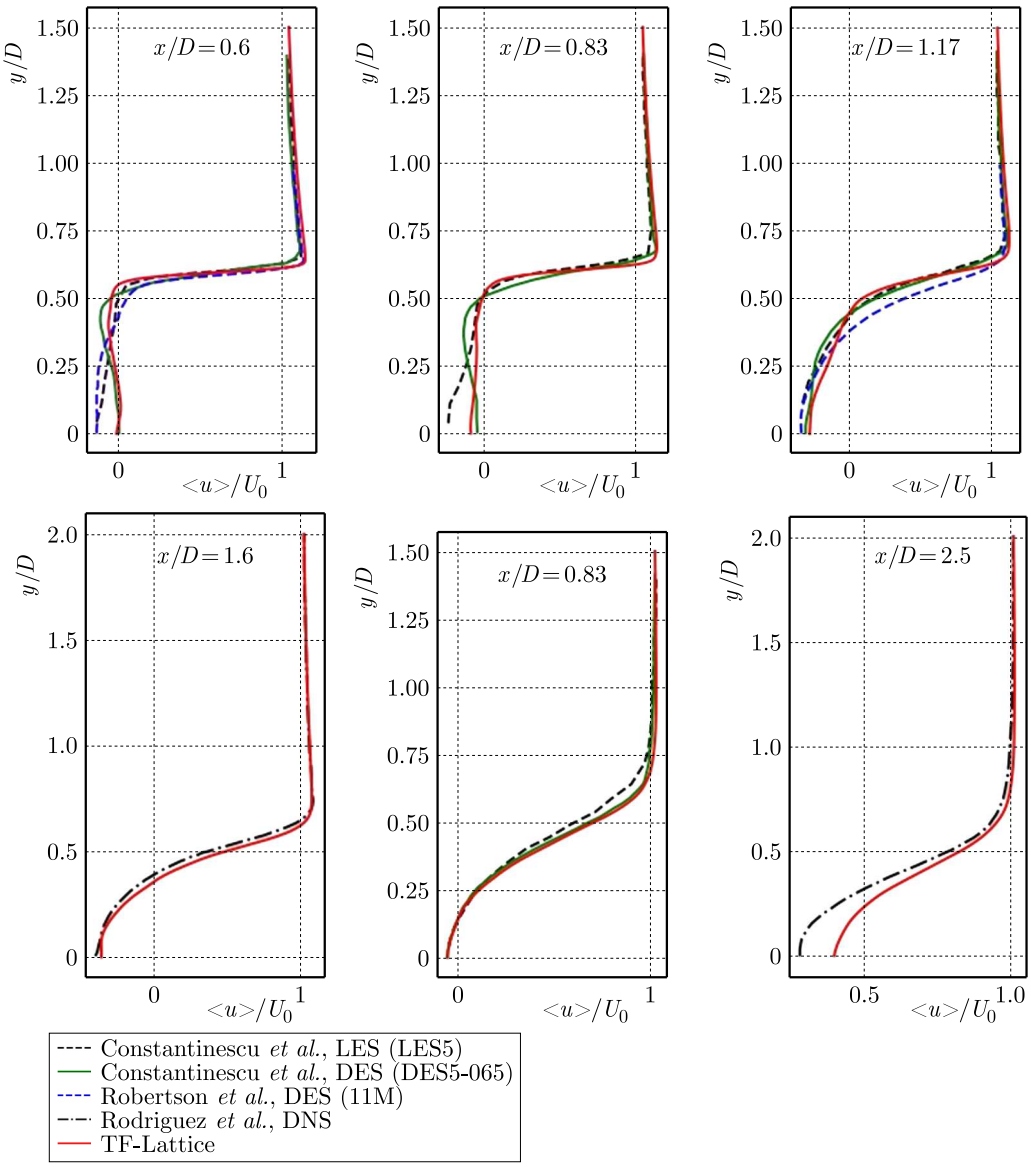

Fig. 15. Average velocity profiles of the fluid flow past a sphere (Re = 10000) at varying distances from the sphere rear: $x = 0.6D$, $0.83D$, $1.17D$, $1.6D$, $2.0D$, $2.5D$

Table 7. Drag coefficient of the cylinder at Reynolds number 10000

Reference example	Method	C_D	Lr/D
Achenbach	Experiment	0.4	–
Ozgoren	Experiment	–	1.4
Rodriguez	DNS	0.402	1.657
Yun	LES	0.393	1.364
Const. & Squires	LES, DES	0.393, 0.397	1.55, 1.48
Robertson	DES	0.393	–
Stiebler	LES (LBM-MRT)	0.443	–
Eitel-Amor	LES (LBM-MRT)	0.392	1.788
Geier	ILES (LBM-Cum.)	0.430	–
TF-Lattice	ILES (LBM-iHRR)	0.397	1.539

A.3.4. DrivAer tests

DrivAer (Heft *et al.*, 2012) is a hybrid model, combining features from both the Audi A4 and BMW 3 Series. This model was designed to advance numerical calculations and experimental methods in vehicle aerodynamics. TF-Lattice uses 8 layers and a total of 22 million grid points to simulate the Notchback and Estateback cases.

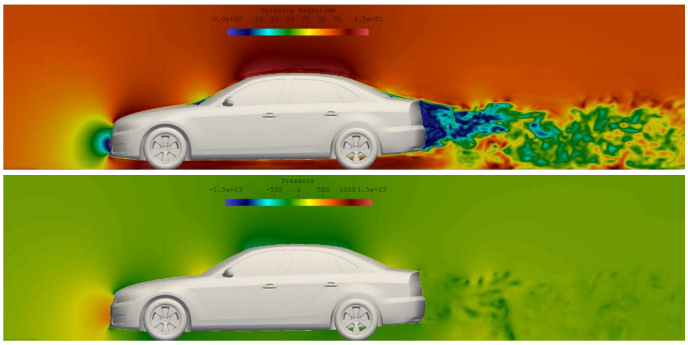

Fig. 16. Instantaneous flow field of the Notchback case (NSwMwWwGS, Heft *et al.*, 2012). The upper figure presents the velocity magnitude field, the lower figure presents the pressure flied

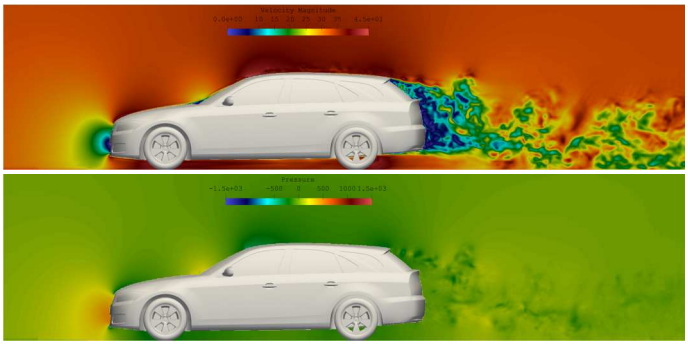

Fig. 17. Instantaneous flow field of the Estateback case (ESwMwWwGS, Heft *et al.*, 2012). The upper figure presents the velocity magnitude field, the lower figure presents the pressure flied

In addition to the exhibited test cases, TF-Lattice has conducted a large number of tests to validate and verify its accuracy and reliability.

Table 8. Drag coefficient of DrivAer

C_D	TF-Lattice	Experiment	Error
NSwMwWwGS	0.2386	0.246	3.0%
ESwMwWwGS	0.2939	0.292	0.7%

Acknowledgement

Special thanks to Tianjin Key Laboratory of Automotive Wind Tunnel Testing and Application and Tenfong Technology for their support and services.

References

1. Ahmed S.R., Ramm G., Faltin G., 1984, Some salient features of the time-averaged ground vehicle wake, *SAE Technical Paper Series*, DOI: 10.4271/840300
2. Bayraktar I., Landman D., Baysal O., 2001, Experimental and computational investigation of Ahmed body for ground vehicle aerodynamics, *SAE Technical Paper Series*, DOI: 10.4271/2001--01-2742
3. Bhatnagar P.L., Gross E.P., Krook M., 1954, A model for collision processes in gases. I. Small amplitude processes in charged and neutral one-component systems, *Physical Review*, **94**, 3, 511-525
4. Chen S., Doolen G.D., 1998, Lattice Boltzmann Method for fluid flows, *Annual Review of Fluid Mechanics*, **30**, 329-364
5. ERCOFTAC Knowledge Base Wiki, page "Ahmed body", 2023, https://kbwiki.ercoftac.org/w/index.php/Abstr:Ahmed_body
6. Fares E., 2006, Unsteady flow simulation of the Ahmed reference body using a lattice Boltzmann approach, *Computers and Fluids*, **35**, 8-9, 940-950
7. Gilliéron P., Chometon F., 1999, Modelling of stationary three-dimensional separated air flows around an Ahmed reference model, *ESAIM: Proceedings*, **7**, 173-182
8. Han T., 1989, Computational analysis of three-dimensional turbulent flow around a bluff body in ground proximity, *AIAA Journal*, **27**, 9, 1213-1219
9. He X., Luo L.-S., 1997, Theory of the lattice Boltzmann method: from the Boltzmann equation to the lattice Boltzmann equation, *Physical Review E*, **56**, 6, 6811
10. Heft A.I., Indinger T., Adams N.A., 2012, Introduction of a new realistic generic car model for aerodynamic investigations, *SAE Technical Paper Series*, DOI: 10.4271/2012-01-0168
11. Hinterberger C., García-Villalba M., Rodi W., 2004, Large eddy simulation of flow around the Ahmed body, [In:] *The Aerodynamics of Heavy Vehicles: Trucks, Buses, and Trains, Conference Proceedings*, McCallen R., Browand F., Ross J. (Eds.), *Lecture Notes in Applied and Computational Mechanics*, **19**, Springer, 77-87
12. Holman D.M., Brionnaud R.M., Abiza Z., 2012, Solution to industry benchmark problems with the Lattice-Boltzmann code Xflow, *European Congress on Computational Methods in Applied Sciences and Engineering (ECCOMAS 2012)*, Eberhardsteiner J. *et al.* (Eds.), Vienna, Austria
13. Jacob J., Malaspinas O., Sagaut P., 2018, A new hybrid recursive regularised Bhatnagar--Gross-Krook collision model for lattice Boltzmann method-based large eddy simulation, *Journal of Turbulence*, **19**, 11-12, 1051-1076
14. Johnson T.A., Patel V.C., 1999, Flow past a sphere up to a Reynolds number of 300, *Journal of Fluid Mechanics*, **1999**, 378, 19-70
15. Keating A., Shock R., Chen H., 2008, Lattice Boltzmann simulations of the unsteady flow behind the Ahmed body, *SAE Technical Paper Series*, DOI: 10.4271/2008-01-0740

16. Keogh J., Barber T., Diasinos S., Doig G., 2016, The aerodynamic effects on a cornering Ahmed body, *Journal of Wind Engineering and Industrial Aerodynamics*, **154**, 34-46

17. Kotapati R., Keating A., Kandasamy S., Duncan B., Shock R., Chen H., 2009, The Lattice-Boltzmann-VLES method for automotive fluid dynamics simulation, *Review, SAE Technical Paper Series*, DOI: 10.4271/2009-26-0057

18. Lienhart H., Becker S., 2003, Flow and turbulence structure in the wake of a simplified car model, *SAE Technical Paper Series*, DOI: 10.4271/2003-01-0656

19. Malaspinas O., 2015, Increasing stability and accuracy of the lattice Boltzmann scheme: recursivity and regularization, *ArXiv preprint*, 1505.06900

20. Nagata T., Nonomura T., Takahashi S., Mizuno Y., Fukuda K., 2016, Investigation on subsonic to supersonic flow around a sphere at low Reynolds number of between 50 and 300 by direct numerical simulation, *Physics of Fluids*, **28**, 5, 056101

21. Qian Y.-H., d'Humières D., Lallemand P., 1992, Lattice BGK models for Navier-Stokes equation, *Europhysics Letters*, **17**, 6, 479-484

22. Schiller L., Naumann A.Z., 1933, Uber die grundlegenden Berechnungen bei der Schwerkraftaufbereitung, *Vereines Deutscher Ingenieure*, **77**, 318-320

23. Sheard G.J., Hourigan K., Thompson M.C., 2005, Computations of the drag coefficients for low-Reynolds-number flow past rings, *Journal of Fluid Mechanics*, **526**, 257-275

24. Strachan R.K., Knowles K., Lawson N.J., 2007, The vortex structure behind an Ahmed reference model in the presence of a moving ground plane, *Experiments in Fluids*, **42**, 5, 659-669

Manuscript received January 5, 2024; accepted for print August 5, 2024